



AFCEC-CX-TY-TP-2016-0003

A SELF-POWERED THIN-FILM RADIATION DETECTOR USING INTRINSIC HIGH-ENERGY CURRENT (HEC) (AUTHOR'S FINAL VERSION)

Piotr Zygmandski

Department of Radiation Oncology Brigham and Women's Hospital
Dana-Farber Cancer Institute and Harvard Medical School
Boston, MA 02115

Erno Sajo

University of Massachusetts Lowell
Department of Physics and Applied Physics
Medical Physics Program
Lowell, MA 01854

Contract No. FA8051-15-P-0010

November 2015

DISTRIBUTION A. Approved for public release; distribution unlimited.
AFCEC-201563; 5 Dec 2015

**AIR FORCE CIVIL ENGINEER CENTER
READINESS DIRECTORATE**

REPORT DOCUMENTATION PAGE

Form Approved
OMB No. 0704-0188

The public reporting burden for this collection of information is estimated to average 1 hour per response, including the time for reviewing instructions, searching existing data sources, gathering and maintaining the data needed, and completing and reviewing the collection of information. Send comments regarding this burden estimate or any other aspect of this collection of information, including suggestions for reducing the burden, to Department of Defense, Washington Headquarters Services, Directorate for Information Operations and Reports (0704-0188), 1215 Jefferson Davis Highway, Suite 1204, Arlington, VA 22202-4302. Respondents should be aware that notwithstanding any other provision of law, no person shall be subject to any penalty for failing to comply with a collection of information if it does not display a currently valid OMB control number.

PLEASE DO NOT RETURN YOUR FORM TO THE ABOVE ADDRESS.

1. REPORT DATE (DD-MM-YYYY) 16 Nov 2015			2. REPORT TYPE Journal Article - Author's Final Version		3. DATES COVERED (From - To) 10 Dec 14 -- 5 Oct 15	
4. TITLE AND SUBTITLE A self-powered thin-film radiation detector using intrinsic high-energy current (HEC) (Author's Final Version)			5a. CONTRACT NUMBER FA8051-15-P-0010 5b. GRANT NUMBER 5c. PROGRAM ELEMENT NUMBER 655025F 5d. PROJECT NUMBER 5e. TASK NUMBER 5f. WORK UNIT NUMBER A00N			
6. AUTHOR(S) ^Piotr Zygmandski, *Erno Sajo						
7. PERFORMING ORGANIZATION NAME(S) AND ADDRESS(ES) ^Department of Radiation Oncology Brigham and Women's Hospital Dana-Farber Cancer Institute and Harvard Medical School			*University of Massachusetts Lowell Department of Physics and Applied Physics Medical Physics Program Lowell, MA 01854		8. PERFORMING ORGANIZATION REPORT NUMBER	
9. SPONSORING/MONITORING AGENCY NAME(S) AND ADDRESS(ES) Air Force Civil Engineer Center Readiness Directorate Requirements and Acquisition Division 139 Barnes Drive, Suite 1 Tyndall Air Force Base, FL 32403-5323			10. SPONSOR/MONITOR'S ACRONYM(S) AFCEC/CXA 11. SPONSOR/MONITOR'S REPORT NUMBER(S) AFCEC-CX-TY-TP-2016-0003			
12. DISTRIBUTION/AVAILABILITY STATEMENT Distribution A: Approved for public release; distribution unlimited.						
13. SUPPLEMENTARY NOTES Document contains color images. Ref Public Affairs Case # AFCEC-201563, 5 Dec 2015. Published in Medical Physics, 2016 Jan;43(1):4. doi: 10.1118/1.4935531.						
14. ABSTRACT A new radiation detection method relies on high-energy current (HEC) formed by secondary charged particles in the detector material, which induces conduction current in an external readout circuit. Direct energy conversion of the incident radiation powers signal formation without need for external bias voltage or amplification. The detector is a thin-film multilayer device, composed of alternating disparate electrically conductive and insulating layers. The optimal design of HEC detectors consists of micro- or nanoscopic structures. Theoretical and computational developments are presented to illustrate the salient properties of the HEC detector and to demonstrate its feasibility. In this work, we examine single-sandwiched and periodic layers of Cu and Al, and Au and Al, ranging in thickness from 100 nm to 300 µm and separated by similarly sized dielectric gaps, exposed to a 120-kVp x-ray beam (half-value thickness of 4.1 mm of Al). The energy deposition characteristics and high-energy current were determined using radiation transport computations. In a dual-layer configuration the signal is in the measurable range. For a defined total detector thickness in a multilayer structure the signal sharply increases with decreasing thickness of the high-Z conductive layers. This paper focuses on the computational results; a companion paper reports the experimental findings. Significant advantages of the device are that it does not require an external power supply and amplification to create a measurable signal; it can be made in any size and geometry, including very thin (submillimeter to submicron) flexible curvilinear forms, and it is inexpensive. Potential applications include medical dosimetry (both in-vivo, and external), radiation protection, and other settings where one or more of the above qualities are desired.						
15. SUBJECT TERMS Auger, direct conversion, electron current, high-energy current, photocurrent, radiation detection, self-powered, thin-film						
16. SECURITY CLASSIFICATION OF: a. REPORT U b. ABSTRACT U c. THIS PAGE U			17. LIMITATION OF ABSTRACT SAR	18. NUMBER OF PAGES 17	19a. NAME OF RESPONSIBLE PERSON Dr. Joseph Wander 19b. TELEPHONE NUMBER (Include area code)	

A Self-powered thin-film radiation detector using intrinsic high-energy current (HEC)

Piotr Zygmanski¹ and Erno Sajo²

5 ¹Department of Radiation Oncology, Brigham and Women's Hospital, Dana-Farber Cancer Institute
and Harvard Medical School, Boston, MA 02115

²University of Massachusetts Lowell, Department of Physics and Applied Physics,
Medical Physics Program, Lowell, MA 01854

- 10 **Purpose:** We introduce a radiation detection method that relies on high-energy current (HEC) formed by secondary charged particles in the detector material, which induces conduction current in an external readout circuit. Direct energy conversion of the incident radiation powers the signal formation without the need for external bias voltage or amplification. The detector we consider is a thin-film multilayer device, composed of alternating disparate electrically conductive and insulating layers. The optimal design of HEC detectors consists of micro- or nanoscopic structures.
- 15 **Methods:** Theoretical and computational developments are presented to illustrate the salient properties of the HEC detector and to demonstrate its feasibility. In this work, we examine single-sandwiched and periodic layers of Cu and Al, and Au and Al, ranging in thickness from 100 nm to 300 μ m and separated by similarly sized dielectric gaps, exposed to 120 kVp x-ray beam (half-value thickness of 4.1 mm of Al). The energy deposition characteristics and the high-energy current were determined using radiation transport computations.
- 20 **Results:** We found that in a dual-layer configuration the signal is in the measurable range. For a defined total detector thickness in a multilayer structure the signal sharply increases with decreasing thickness of the high-Z conductive layers. This paper focuses on the computational results while a companion paper reports the experimental findings.
- 25 **Conclusions:** Significant advantages of the device are that it does not require external power supply and amplification to create a measurable signal; it can be made in any size and geometry, including very thin (sub-millimeter to submicron) flexible curvilinear forms, and it is inexpensive. Potential applications include medical dosimetry (both *in-vivo*, and external), radiation protection, and other settings where one or more of the above qualities are desired.
- 30 **Keywords:** radiation detection, electron current, high-energy current, direct conversion, Auger, photocurrent, self-powered, thin-film

35 Introduction

- 35 Radiation detectors convert the energy of radiation to discernible signal by various direct or indirect mechanisms. Their common feature is that the energy is deposited in the active bulk medium of the device, which produces other types of intermediate carriers of energy to facilitate the formation of the detectable signal¹. For instance, in conventional indirect-conversion detectors x-ray energy is imparted to an active medium, such as a scintillator or a latent material (e.g., photo-stimulated phosphor), and another device (e.g., photodiode) is used to read the secondary light emission originating in or passing through the medium. By contrast, in direct-conversion detectors radiation interactions produce charge carriers (electron-hole pairs or ion pairs) whose collection typically requires an externally applied strong electric field (e.g., bias voltage), which transports the charges across the active medium to form a signal in an external circuit. Conversion of energy via multiple mechanisms invariably results in loss of efficiency, increased complexity, and higher production and operation costs. It may also prevent miniaturization and reduction of the power consumption, thus leading to an inability to make the device practical in certain applications.

- 50 In this paper we describe, and propose for medical applications, a different type of conversion of radiation to detectable signal, which does not require external bias voltage and which is most efficient when used in multilayer nanostructured design. This detector uses the energy of the incident radiation to provide a detectable signal without need for amplification. The principles of operation of this device are quite different from the conventional technology and require rethinking of the underlying assumptions and potential applications. Herein we present the main concept and illustrate it via radiation transport computations in multilayer thin-film structures. A prototype radiation detector employing the proposed energy conversion scheme is described in a companion paper².

Materials and Methods

55

When a high atomic number (high-Z) conductor is exposed to x-rays below about 0.5 MeV, the secondary electrons are predominantly photoelectrons and Auger electrons. Similar effects are expected for other primary radiation types (e.g., electron beam) via knock-on ionization of inner shell electrons³. When at least one of a pair of conductor dimensions is small compared to the secondary charged particle range, this leads to a high-energy electron current (HEC) that leaks into the low-Z medium separating the conductors (interstitial medium). In our design the interstitial medium may be a void or filled with gas (air), or a solid (dielectric) in a sandwiched configuration (Fig 1A), or it may have a multilayered structure (Fig 1B). The primary energy loss of the incident beam occurs in the high-Z layers, followed by ejection of secondary electrons, which naturally constitute the extremely mobile charge carriers moving in the low-Z layers. This phenomenon can be described from different perspectives using parallels, e.g., by characterizing the interstitial medium as insulator for low-energy but conductor for high-energy electrons. In layered structures, there is a combination of secondary electrons and photons in forward and reverse directions. The disparate metal layers form a resonant cavity, in which secondary fluorescent photons give rise to further photoelectrons and Auger electrons in an avalanche cascade, in which each generation has a lower energy and higher interaction cross-section. The resultant electron population could be directly utilized to obtain a signal proportional to the intensity of the incident radiation.

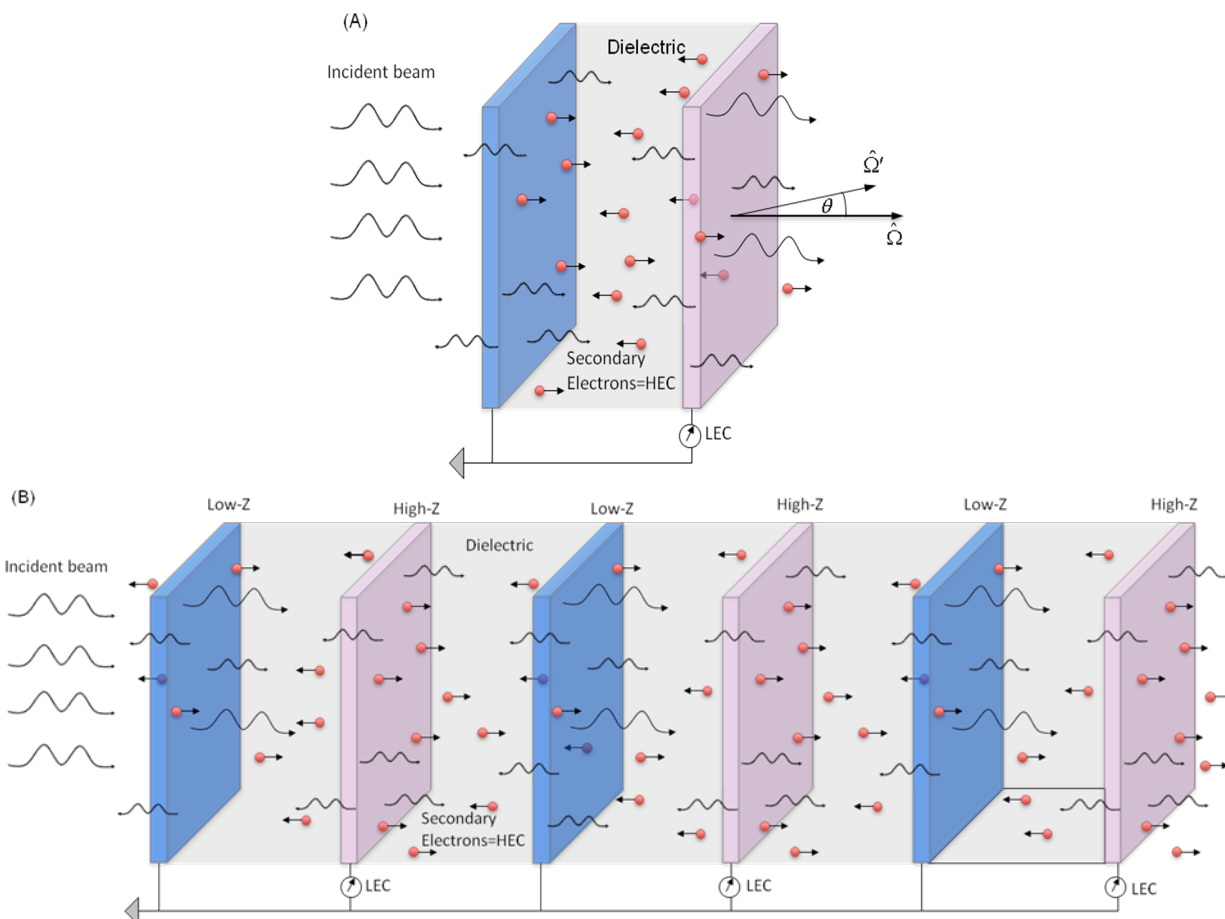


Figure 1 (A) Two conductor layers with disparate atomic numbers separated by dielectric (gaseous or solid) exposed to incident radiation. The high-Z layer acts as emitter (cathode), while the low-Z plate is the collector (anode). The secondary electrons give rise to a net high-energy current (HEC) traversing the low-Z dielectric layer, which in turn induces low-energy (i.e., conduction) current (LEC) in the electric circuit. (B) Multilayer periodic structure composed of alternating high-Z / low-Z conducting layers. The induced LEC is measured for each high-Z layer separately or as the total signal from all the conducting layers. In the diagram, large waves represent incident and uncollided source photons and small waves indicate fluorescent photons. Secondary electrons are shown using red spheres. Because there is greater electron leakage from the high-Z materials, a net HEC is formed from the high-Z towards the low-Z plates. The number of photons and electrons are illustrative only, they do not represent exact contributions.

75

80

85 Photon and neutron interaction-induced secondary electron transfer across dissimilar materials separated by a dielectric is a known phenomenon. Most notably, it has been investigated from the perspective of electromagnetic pulse effects on cables and electrical devices⁴ and as a self-powered detector for in-core neutron flux measurement in nuclear reactors^{5,6}. In all of these studies, the geometry of interest had macroscopic dimensions either because of the nature of the problem (e.g., insulated cables) or because the in-core detector was designed to maximize the neutron or photon absorption in the device. When designed to utilize photon interactions, the underlying operating principle is based on the detection of photocurrent and Compton current⁷⁻⁹ originating in a high-Z electrode. However, in these devices, because of the macroscopic dimensions, there is a significant loss of HEC signal due to self-shielding. In high-flux neutron and photon applications (e.g., nuclear reactor) suppressed detector response to one versus the other radiation type is often beneficial. However, in lower flux conditions microscopic dimensions and multilayer structures may be required to better utilize the HEC. Specifically, when the electrodes are made of thin films, micron- and submicron range, not significantly thicker than the average range of secondary photoelectrons, Auger electrons and Compton electrons, the leakage of charged particles from the high-Z material and across the dielectric interface can be more effectively harnessed. The secondary leakage HEC electrons, which possess relatively high energy compared to conduction electrons, induce an electric current that is detectable without amplification. Measurement of the external current is achieved via similar methods to those used in the conventional detectors, with or without amplification of the raw signal. In the experimental work, reported in our companion paper², we demonstrate that for conventional kVp beams amplification is not necessary. In the present paper we focus on theory and computations of radiation-induced currents in periodic microstructures.

90 05 Although photo-Auger-electron related signal enhancement has been investigated for thin film high-Z structures¹⁸, there are important differences between the HEC concept and the working principles of the dose enhancement based devices. Further, the radiation physics literature does not describe the use of photo-Auger current as the source of quantifiable signal in radiation detectors realized with alternating low-Z/high-Z layered micro- or nano-structures. A more detailed comparison is provided in the Discussion section of this paper.

Theory: The HEC Concept

10 To distinguish the two types of electron currents, conventional electric (i.e., conduction) current versus the current of high-energy electrons secondary to photon interactions, we refer to the latter as HEC and the former as low energy current (LEC). HEC is rooted in radiation transport theory. Consider the angular flux $\Psi(\vec{r}, E, \hat{\Omega}) dE d\hat{\Omega}$, which represents the number of high-energy particles at location \vec{r} moving in the solid angle of $d\hat{\Omega}$ about the direction $\hat{\Omega}$, having energy dE about E , and crossing a unit surface in a unit time. The angular current is defined as $\bar{J}(\vec{r}, E, \hat{\Omega}) = \hat{\Omega} \Psi(\vec{r}, E, \hat{\Omega})$. Several variants of HEC can be derived depending on the desired differential quantities. For example, the net current is the integral of the angular current over all directions, and in spherical geometry it can be expressed in terms of the polar and azimuthal angles (θ, φ):

$$\bar{J}(\vec{r}, E) = \int_{4\pi} \bar{J}(\vec{r}, E, \hat{\Omega}) d\hat{\Omega} = \int_0^{2\pi} \int_{-1}^1 \bar{J}(\vec{r}, E, \hat{\Omega}) d\mu d\varphi \quad (1)$$

15 20 where $\mu = \cos(\theta)$. In planar geometry the net current is the difference between the forward current and the reverse current with respect to the direction of the incident primary photon radiation. A related quantity of leakage current through a surface of interest is

$$j(\vec{r}, E, \hat{\Omega}) = \hat{n} \cdot \bar{J}(\vec{r}, E, \hat{\Omega}) \quad (2)$$

25 25 where \hat{n} is the surface normal. In this way, a net leakage current or flow rate can be obtained using a similar integration as above. In planar geometry where the primary photon beam is plane-parallel normally incident on the surface, the flow rate coincides with the absolute value of the current. In the terminology used in this paper HEC corresponds to the forward, reverse or net leakage currents:

$$j_F(\vec{r}, E) = \int_0^{2\pi} \int_0^1 j(\vec{r}, E, \hat{\Omega}) d\mu d\varphi \quad (3)$$

$$j_R(\vec{r}, E) = \int_{0}^{2\pi} \int_{-1}^0 j(\vec{r}, E, \hat{\Omega}) d\mu d\phi \quad (4)$$

30 The net leakage current is the arithmetic difference (or sum, depending on the sense of the coordinate system) of the forward and reverse leakage currents, equivalent to the integral:

$$j_{net}(\vec{r}, E) = \int_{4\pi} j(\vec{r}, E, \hat{\Omega}) d\hat{\Omega} \quad (5)$$

In a thin film device composed of alternating layers of high-Z electrode, low-Z dielectric, and low- or medium-Z conductor a conduction electron current (LEC) is induced by the net leakage current, HEC. This gives rise to a usable signal in two ways:

- 35 (1) The high-energy leakage current involves energetic electrons (generated primarily by the photoelectric effect followed by Auger emission in this case) that travel from their site of origin (high-Z conductive layer, herein called "cathode") across a non-conductive or poorly conductive medium (e.g., dielectric, semiconductor, vacuum, or gas-filled cavity) towards a conducting collector (medium- or low-Z layer, herein called "anode"). Figure 1 schematically shows examples of secondary electrons and photons in a multilayer structure. Since HEC is generated by photon interactions, it does not require an external electric field to maintain. Although it can be combined with an external field, HEC induces moving charges in the external electric circuit of a sensor on its own, and thus the device is self-powered. We distinguish HEC from the current in the external circuit, which is the standard low-energy electric current such as the current flowing in a medium due to electromotive force or electric field.
- 40 (2) In addition, as HEC traverses the interstitial low-Z dielectric, it can directly ionize the medium and give rise to a multitude of charge carriers (ionized electrons, positive or negative ions, or electron hole pairs), which are self-collected by the contact potential between the high-Z and low-Z conductors, maintaining or amplifying the self-powered nature of the detector.
- 45

50 A device using the HEC mechanism may consist of a single sensor or multiple sensors forming an array. A sensor can be a macroscopic device or a micro/nano-device. Each sensor is composed of a few layers (Fig 1A) or many layers (Fig 1B). Secondary particles produced by primary radiation interactions in the electrodes are photoelectrons, Auger electrons and fluorescent x-rays. For high-Z materials the fluorescent x-ray yield is greater than the Auger yield. However, the secondary x-rays have low energy and they have higher photoelectric interaction cross-section than the incident x-rays, and they mostly stop in the high-Z layers, providing further contribution to the detector signal via a concomitant sequential cascade of further photoelectrons, Auger electrons, and low-energy fluorescent x-rays, resembling a resonant cavity. In the case of thin detector structures with just a few layers, a fraction of fluorescent x-rays is also likely to escape without interactions similarly to the primary incident photons. For multilayer detector structures most of the fluorescent x-rays is absorbed in the active layers. In imaging applications, x-ray fluorescence may lead to decreased spatial resolution when planar geometry is used. Non-planar or structured detector geometries may be pursued in the future to absorb the fluorescent x-rays closer to the primary photon interaction site within the same pixel.

55 The optimum layer width is a balance between adequate thickness to maximize the interaction rate with the incident radiation yet allow the secondary electrons to escape, which superficially appear as two opposing criteria. The next section will show that for a defined total detector thickness in a multilayer structure, the net HEC sharply increases with decreasing thickness of the high-Z conductive layers. Depending on the number of layers, their optimal thickness may be in the nanometer range.

Computer Simulations

70 To illustrate the principles of a HEC device, we assume a planar geometry with a few or more thin electrically conducting parallel layers separated by dielectric gaps. In this paper, we consider two combinations of materials and dielectrics: copper and aluminum separated by SiO_2 or dry air, and gold and aluminum separated by the same dielectrics. The basic characteristics of the net HEC across the layers will be shown, including the effect of varying high-Z layer thickness.

75 In a separate analysis, using a multilayer structure of Au and Al separated by dry air, the effect of the layer thicknesses is examined. While the total thickness of the structure is kept constant at 1300 μm , the thickness of the layers is varied, ranging from 100 nm to 300 μm , permitting a varying number of equidistant layers within the structure. Therefore, in these geometries the total number of layers increases with decreasing layer thickness.

80 For comparison purposes, we also consider homogeneous media as opposed to disparately layered structures. In particular, we examine a uniform and homogeneous mixture of aluminum and gold having the same proportion of constituent elements as the layered structure: 50% Al and 50% Au by thickness, or 0.123 Al and 0.877 Au by weight with effective density of 5.51 g/cm³. The latter is of specific interest, as it is a reference medium to which multilayered structures converge asymptotically.

85 Further, we study the electron spectra in the center of the gap between two conducting layers as a function of gap size. In particular, we assume a structure composed of 3 layers: Al (100 μm) – air / vacuum gap (1 μm -500 μm) – Au(100 μm). The photon spectra at the internal surfaces of the electrodes and in the center of the air gap are also examined and the contribution of the fluorescent photons are highlighted.

90 A plane-parallel photon beam normally incident on the left-hand side of the detector was assumed, as shown in Fig 1B. The photon source was a spectral 120 kVp beam with a half value thickness of 4.1 mm of aluminum. Simulation of radiation interactions with the microscopic and nanoscopic structures was carried out using the CEPXS / ONEDANT deterministic radiation transport computer code¹⁰. The spatial distribution of energy deposition, dose, particle flux spectrum, and net current were computed and analyzed as a function of layer thickness. Net current is the arithmetic difference between the forward and the reverse leakage currents, with respect to the incident photon beam, as shown in Eq.(5).

95 The CEPXS/ONEDANT code package is a deterministic radiation transport computation system consisting of two major modules, CEPXS and ONEDANT. The CEPXS code provides coupled electron-photon cross-sections to be used with the ONEDANT discrete-ordinates radiation transport code. The CEPXS data is organized into a format that converts the discrete ordinates solution of the Boltzmann equation into a solution that uses the restricted continuous-slowing down approximation (CSDA) to represent soft inelastic reactions of electrons and positrons¹⁰. In 00 the restricted CSDA, electrons are assumed to continuously lose energy due to many soft reactions along their path, without angular deflection. By contrast, catastrophic interactions that result in large energy losses and scattering angles are represented by macroscopic cross sections for which a conventional multigroup treatment is used. The ONEDANT code uses the discrete-ordinates method to solve the multi-group Boltzmann transport equation in one-dimension. Owing to the difficulty in treating soft inelastic reactions that have large cross-sections for small energy 05 loss with almost no change in direction, discrete-ordinates transport codes have become available only recently¹¹.

0 The computations presented here include all of the important electron-photon interactions that are normally part of Monte Carlo computations. The cross-sections used by CEPXS are essentially the same as those included in the ITS code system¹², which are also incorporated in many other Monte Carlo models. A summary of interactions 10 considered by CEPXS is provided in the Appendix. An added feature of CEPXS/ONEDANT is that its low-energy cutoff is extended to 100 eV and that it considers Auger transitions up to the N shell, which are often not found in general purpose Monte Carlo codes. The advantage of the discrete-ordinates method over the stochastic Monte 15 Carlo method of solution is that it deterministically solves the coupled Boltzmann's transport equation for photons and electrons in the entire phase space with a nearly arbitrary number of spatial and energy meshes. The computational time is generally a minor fraction of that demanded by Monte Carlo methods, making it suitable for running complex high spatial and energy resolution problems. Further details in the context of medical physics application, including a brief description of the deterministic solution method of the linear Boltzmann equation, are 20 presented by Williams and Sajo²⁴.

25 An assumption in our calculations is that the detector structure and the incident beam can be represented in a planar geometry. The CEPXS/ONEDANT 1-D slab model computes the transverse-integrated flux as a function of depth in the structure for the actual finite-dimension incident beam. Because the incident beam size is larger than the detector area and the lateral size of the detector is orders of magnitude greater than its thickness, the solution is equivalent to one in which the photon beam is modeled as an infinite planar source incident on a slab target region. Therefore from the perspective of simulation fidelity, the 1-D geometry does not significantly depart from the realistic experimental geometry in medical x-ray beams².

Results

Figure 2A shows the computed net HEC across a sandwiched structure, such as illustrated in Fig 1B but terminated

at the second low-Z layer, inclusive. In this example, the low-Z electrodes proximal and distal to the incident radiation are both 5 μm Al, the dielectric is 300 nm SiO_2 , and the central high-Z layer is Cu in various thicknesses. Figure 2B shows a similar structure, except the dielectric layers are 100 μm dry air, each, whose density-thickness is equivalent to 300 nm SiO_2 . Because SiO_2 and Al have similar photon and electron transport properties, the variation of the net HEC is also similar in the two media, exhibiting a nearly continuous smooth transition across the different materials. When the dielectric is air, however, there is an abrupt change across the dissimilar layers and the current is nearly constant across much of the air gap due to the smaller energy loss and absorption of HEC electrons. It is further seen that in this particular structure the optimal Cu layer thickness is approximately 5 μm . Below this thickness the layer is too thin to have adequate interaction density with the incident photons while above this thickness gradually fewer secondary electrons can escape from the material due to self-shielding.

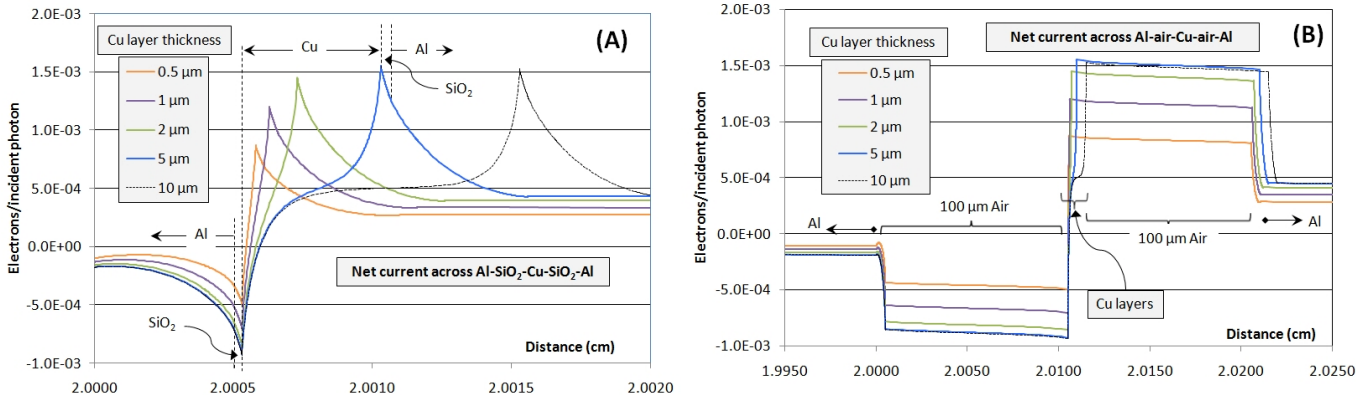


Figure 2. (A): Net electron leakage current (HEC) across an Al-SiO₂-Cu-SiO₂-Al structure. Both Al layers are 5 μm and both SiO₂ layers are 300 nm while the Cu layer is varied as indicated. The structure is embedded in 2 cm of air on both sides, therefore the abscissa starts at 2 cm. Plane-parallel 120 kVp x-rays are normally incident on the left. (B) The same structure as in (A) but each 300 nm SiO₂ layer is replaced by an equivalent density-thickness of dry air, 100 μm . Negative net current indicates that more electrons are moving in the reverse (opposite to the direction of the incident photon beam) than in the forward direction.

Figure 3 compares the leakage HEC on the left and right-hand sides of the central high-Z layer when the layer material is Cu versus Au. The irradiation conditions and the Al and dielectric layers are identical to those shown in Fig 2. For each comparable layer thickness, using Au instead of Cu as the central electrode results in approximately three times greater leakage current in absolute value. The optimal thickness of the Au electrode in this geometry is about 2 μm . In each case, Cu and Au, the maximum HEC near the central electrode boundary are similar, irrespective of the material of the dielectric owing to their equivalent density-thickness. For example, for a 2 μm Au layer the HEC is $\sim 4.38 \cdot 10^{-3}$ electrons/incident photon on the distal side regardless of the material of the dielectric. In the case of 5 μm Cu, this value is $\sim 1.53 \cdot 10^{-3}$ electrons/incident photon.

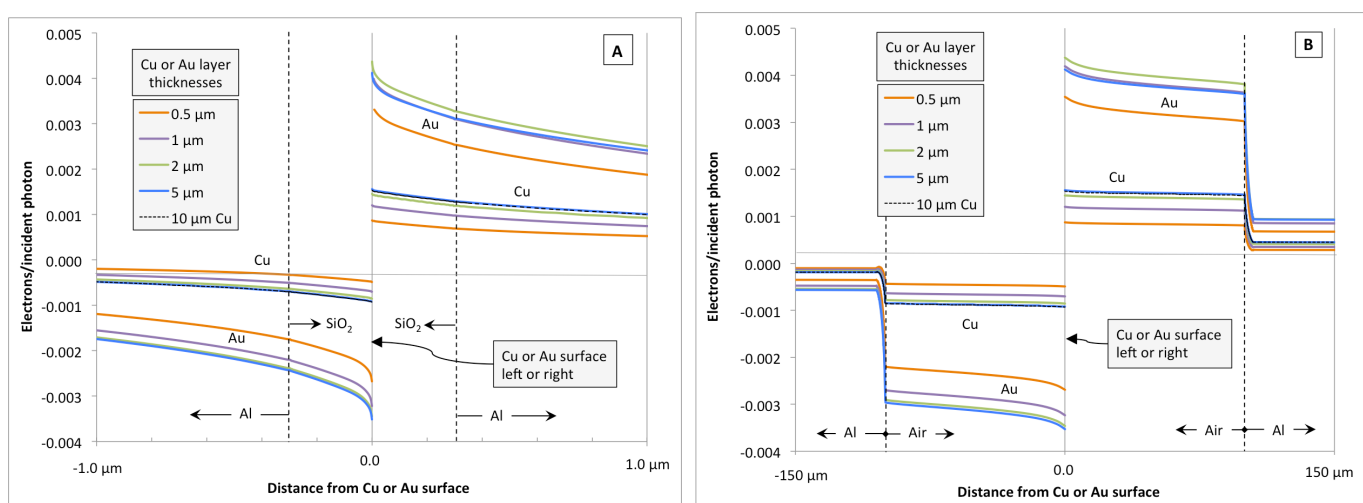


Figure 3. HEC on the proximal and distal sides of the central high-Z electrode in the design examined in Fig.2. and when the Cu electrode is replaced by an Au electrode in similar thickness. (A) uses SiO_2 while (B) employs air as dielectric. The left and right boundaries of the Al layers are beyond the limits of the figures.

For a constant total structure thickness, increasing the number of layers in a multilayer structure (and concomitantly reducing the size of the individual layers) dramatically increases the harvestable HEC. Figure 4 illustrates this by splitting the 2- μm central Au layer employed in the above analysis to two 1- μm layers. While in a single sandwiched layer of Al-dielectric-Au-dielectric-Al 2 μm appears to be the optimal Au thickness to produce the highest HEC, in a dual-sandwiched structure of Al-d-Au-d-Al-d-Au-d-Al, two 1- μm Au layers achieve nearly the same magnitude of HEC for each Au electrode, almost doubling the harvestable signal.

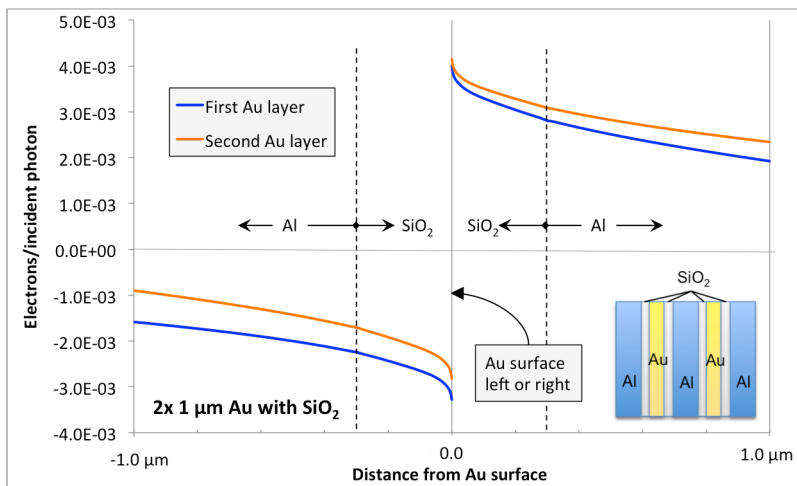


Figure 4. HEC on the two sides of two 1- μm layers of Au in a dual-sandwiched structure Al- SiO_2 -Au- SiO_2 -Al- SiO_2 -Au- SiO_2 -Al whose total thickness is the same as the single-sandwiched structures examined in Figures 2 and 3. The harvestable HEC is effectively doubled.

In this way, increasing the number of high-Z layers while decreasing their thickness to as low as a few hundred nanometers, which is comparable to the mean range of secondary electrons born in this layer, can substantially increase the overall efficiency of the detector. Because the HEC detector has no restriction on employing certain materials in the active sensor, e.g., lead (Pb), such multilayer structure can possess the same and even significantly higher beam absorption fractions as current state-of-the-art detectors while retaining its ability to harvest signal from multiple layers.

HEC as a function of distance from the electrodes exhibits several unique features: (1) the net particle current flows from the high-Z electrode to the low-Z electrode, (2) which is larger for high-Z materials. (3) in the dielectric layer, there is a decrease of the leakage current with distance from the high-Z surface due to the large component of low-energy short-range electrons (mostly Auger), which leads to higher ionization density near the surface. Figure 5 shows examples of dose distribution as a function of distance for two extreme cases of microscopic (100 μm) and nanoscopic (100 nm) layers of Al-air-Au in a stacked geometry as shown in Fig 1B. In both cases the total thickness of the structures is 1300 μm . Doses in multilayered HEC structures are compared to doses in equivalent homogeneous media having the same elemental proportion of gold and aluminum as the layered structures. Remarkably, in the 100 nm structure the dose in gold, but not in the other layers, is very similar to that seen in the homogeneous mixture. In contrast, the 100 μm structure exhibits large deviations of dose in the layered versus homogeneous medium due to greater attenuation in the gold. When the layers' thickness is comparable to the range of the leakage electrons there is a characteristic pattern of higher dose in low-Z materials and lower dose in high-Z materials due to electrons leaking from the high-Z material and depositing their energy in the low-Z material. By contrast, when the layers are relatively thick, most of the secondary electrons will deposit in the high-Z layer.

Figure 6 displays the net HEC (Eq.5) as function of distance from the proximal face of the structure with respect to the incident photons, corresponding to the same cases as shown in Figure 5. The net HEC exhibits a characteristic oscillation between high-Z and low-Z layers. There is a net electron leakage from the high-Z layer, which cannot be compensated by leakage originating in the low-Z layer. By contrast, in the homogeneous mixture the net HEC is a relatively smooth function of distance.

Figure 7 shows the net HEC for 25 μm layers of Al and Au as a function of distance, exhibiting a similar behavior as shown above. When the net current in the multilayer structure is normalized to the net current in the homogeneous mixture (50% Au + 50% Al by thickness) (Figure 7C) the oscillations of the normalized net current from layer to layer show little dependence on depth, suggesting that the attenuation seen in Figure 6A are primarily due to the attenuation of x-rays.

Figure 8 examines the role of the layer thickness in the Al-air-Au-etc multilayer device with a constant total thickness. The total net current in the entire detector, which is the sum of leakage currents for all high-Z (Au) conducting layers, is plotted against the layer thickness. The leakage current for a given layer is computed as a sum of leakage currents on the two opposite sides of that layer. It is seen that the effectiveness of the HEC structure is the greatest for thin layers as the total current exponentially decreases with increased layer thickness. Therefore, in stark contrast to conventional detectors where the device efficiency increases with increased size, the efficiency of a multilayer HEC device increases with reduced layer thickness.

Electron spectra at the center of air gap in a single-sandwiched structure (Al - air – Au, similar to Fig. 1A) are compared to the spectra for air-free gap (vacuum) in Figure 9. The composition of secondary electrons due to the incident 120 kVp photon beam is primarily photoelectrons and Auger electrons, and to a lesser extent Compton electrons. Auger electrons originating in gold have an increasing presence below 10 keV and are dominant below 3.7 keV. Vacuum represents a limiting condition in the dependence on both gap size and fill gas properties. Comparison as a function of air gap size (1 μm -500 μm) reveals that the Auger electrons are gradually absorbed as the air gap becomes larger. However even at 100 μm gap size the Auger electrons are still present.

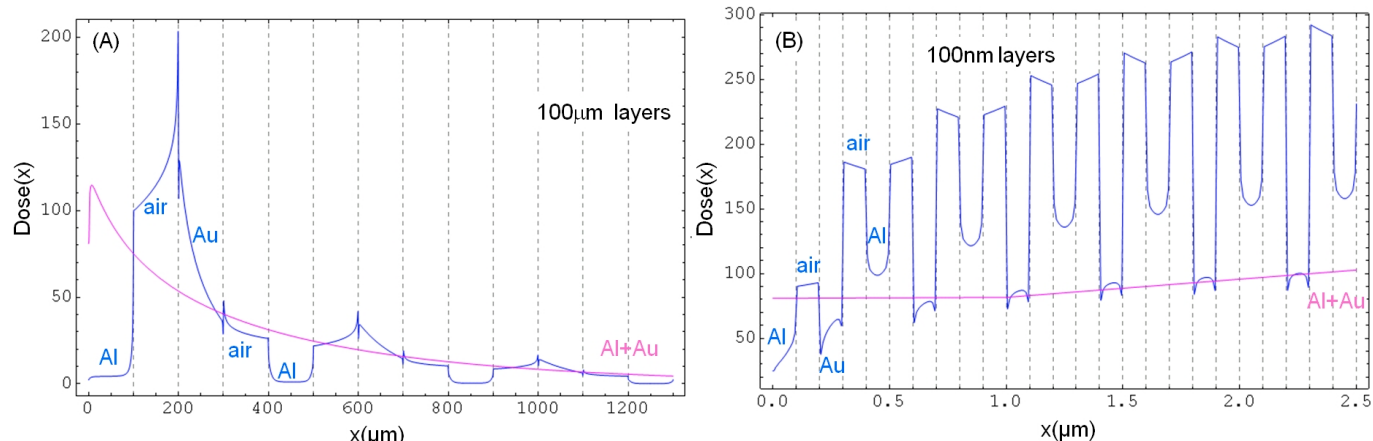


Figure 5. Normalized dose (ratio of dose in detector to dose in water medium) as a function of position in multilayered HEC structures employing repeated Al-air-Au assemblies versus in a uniform homogeneous mixture of Au and Al with the same elemental proportion by volume as in the layered structure: (A) 100 μm layers and (B) 100 nm layers. For thicker layers the absorption in gold dominates. In (B) only the initial layers within the first few microns are shown. The simulations used a plain-parallel beam of 120 kVp spectral x-ray source, normally incident on the left side of the structure.

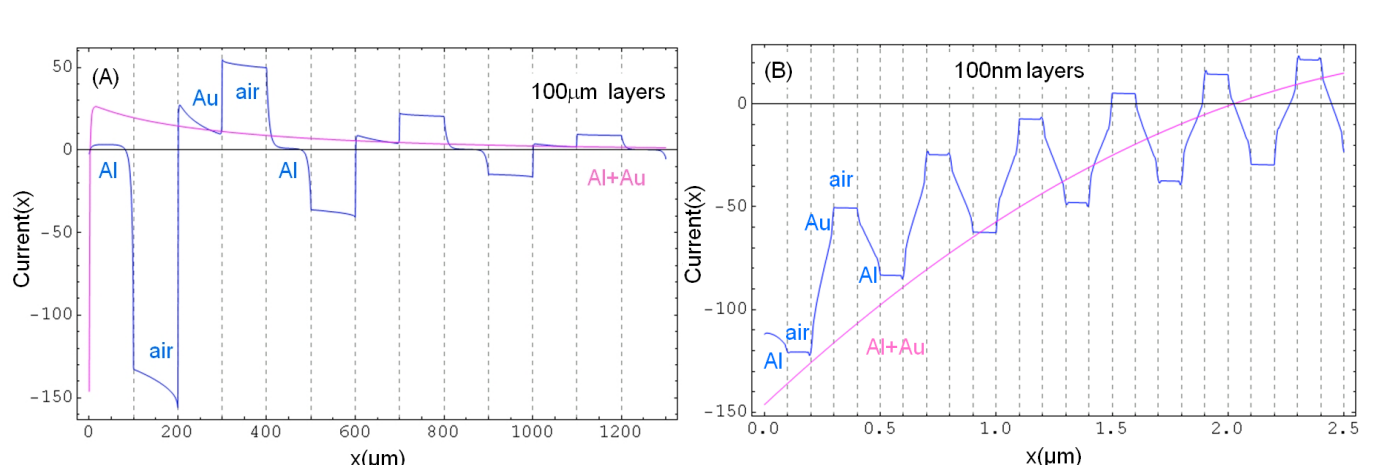
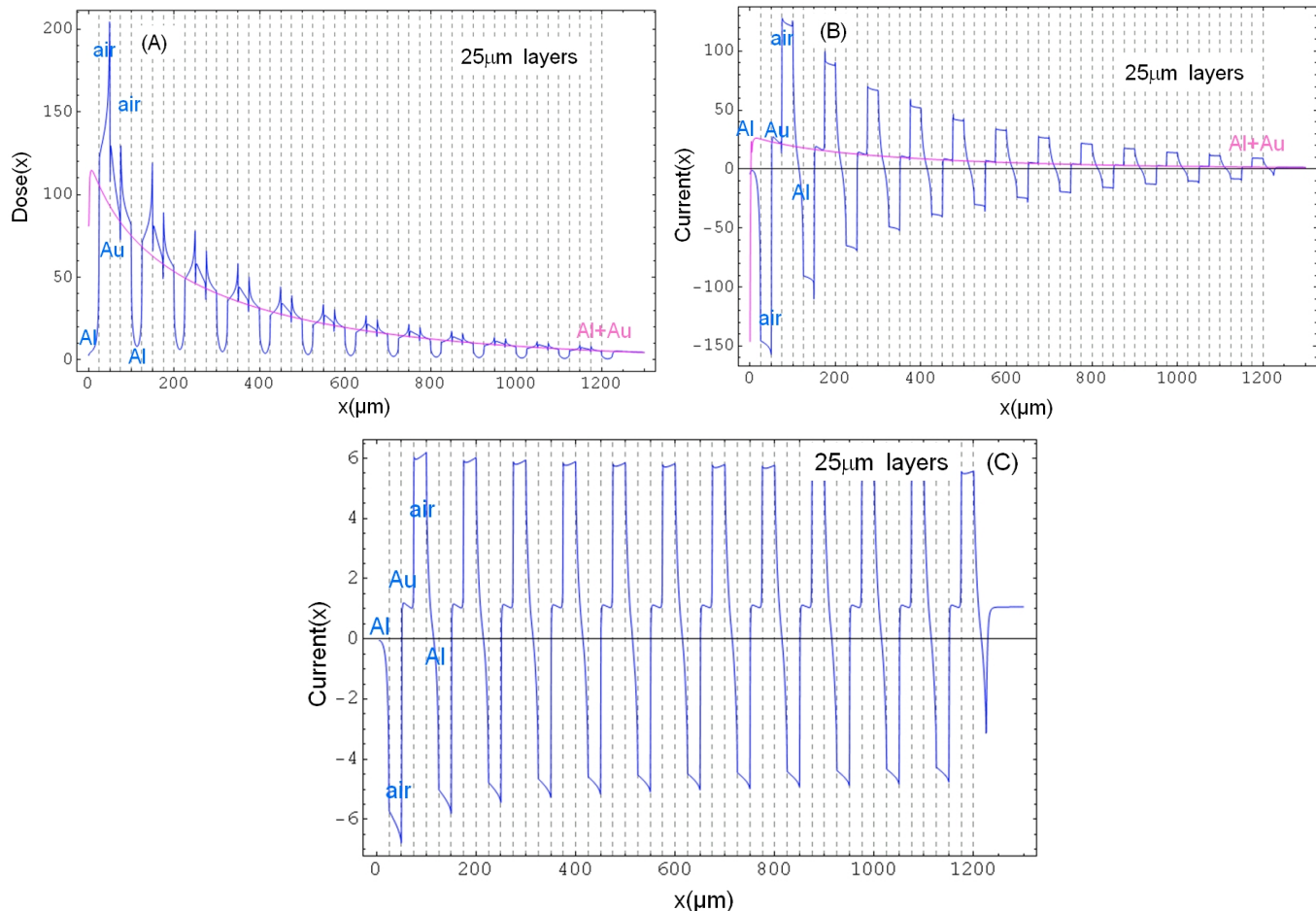
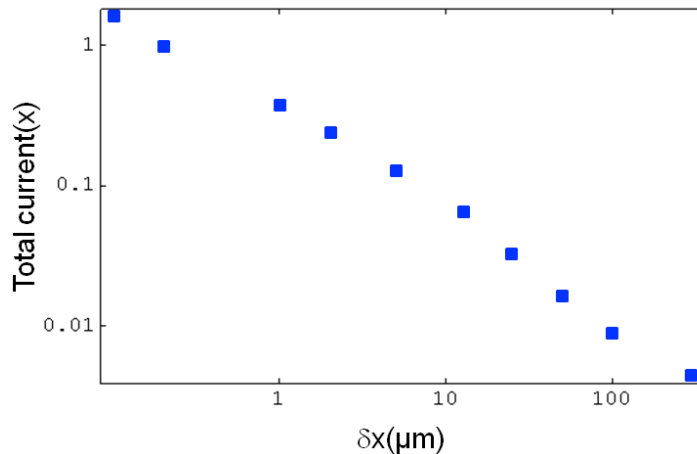


Figure 6. Net normalized HEC as a function of distance for the same structures as in Figure 5.



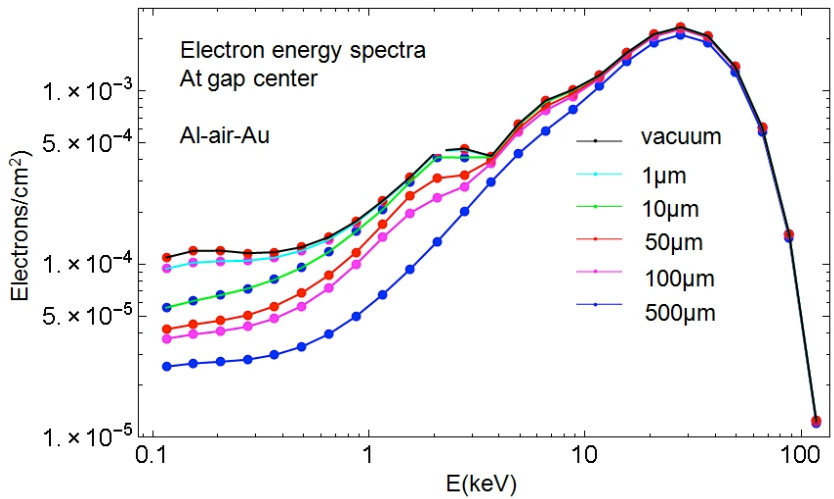
30

Figure 7. Attenuation of normalized dose (A) and net HEC (B) across a multilayer structure with 25 μm repeated layers of Al, air, and Au, each. When the current is normalized to the current computed in the homogeneous mixture of Au and Al (C) the proximal and distal currents leaking from high-Z layers are proportional to the x-ray intensity at a given depth inside the structure. The computations used the same irradiation conditions as above.

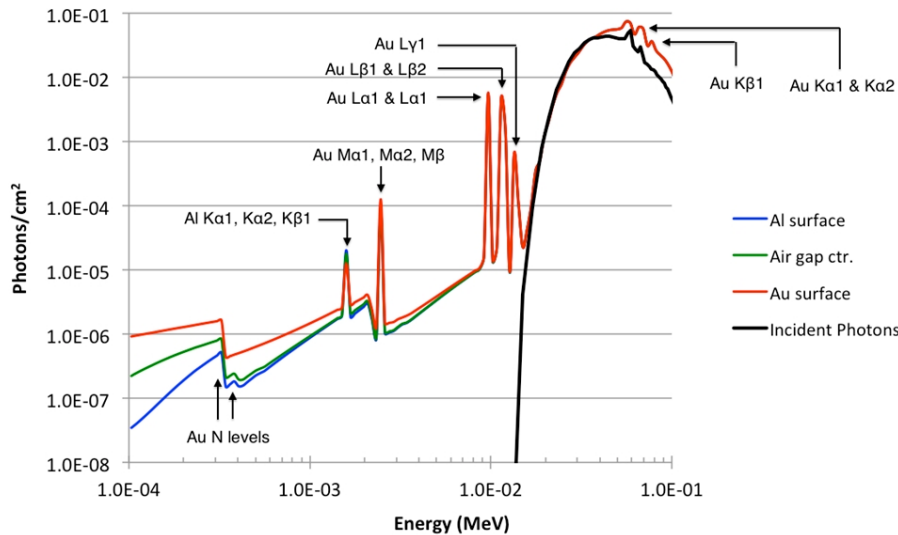


35

Figure 8. Dependence of the total (relative) current harvested from all layers of the entire device as a function of layer thickness, δx . The total current is the sum of net leakage currents for all high-Z conducting layers, which are made of Au in this study.



40 **Figure 9.** Electron flux spectra at the center of gap in Al(100 μm)-gap(parameter)-Au(100 μm) structure for various gap sizes, normalized to one photon incident on the surface of the detector. The gap is filled with dry air (1 μm – 500 μm) or vacuum. The electron spectrum in vacuum is independent of the gap size. Incident beam is plane parallel 120 kVp x-rays.



45 **Figure 10.** Photon spectra inside the same dual-layered Al-air-Au structure as in Fig. 9. 120 kVp photon spectrum (black) is normally incident on the Al layer from the left. The generated spectra are shown at the inside of the Al surface (blue), in the center of the air gap (green) and in the inside surface of the Au layer (red). The fluorescent emission lines are labeled.

50 Figure 10 displays the photon spectra at three locations in the same Al-air-Au structure: at the inside Al surface, in the center of the air gap and at the inside of the Au surface. There is a significant production of secondary fluorescent photons, which are identified in the figure. The presence of the thin air gap impacts only the lowest energy photons, below 3 keV. Beyond the initial photoelectric reactions by source photons, a cascade of secondary electron emission is generated due to the low-energy fluorescent photons interacting with higher shell electrons in the two metal plates. For example, the gold M-series fluorescent lines (2.1-2.2 keV) have high photoabsorption cross-sections with the aluminum K-shell electron (1.6 keV). The Al K-series lines (1.48-1.55 keV) can interact with the Au N-shells (0.084-0.762 keV), and the Au L lines (9.6 and 9.7 keV) interact with the Au M shells (2.2-3.4 keV) and also with the Al K shell (1.56 keV). This generates a multiple and sequential cascade of photoelectron and Auger electron emission.

55 50 Discussion

The HEC concept

65 In understanding the HEC concept the notions of what is “direct” versus “indirect”, and “active” versus “passive” relying on preconceptions afforded by traditional radiation detectors may be misleading.

70 Compared to Compton- and photocurrent based devices, such as in-core nuclear reactor instrumentation, the HEC concept uses an additional, thus far underutilized, radiation conversion mechanism of Auger electrons, which is possible to harness only when the electrodes and dielectrics are very thin. Even though most of the Auger electrons have relatively low energies, there are many emission lines above 1 keV, depending on the selected high-Z material, which have a significant contribution to HEC when the high-Z cathode is sufficiently thin to prevent self-absorption. Compared to the conduction electrons, Auger, Compton, and photoelectrons possess much higher energy, capable of traversing thin low-Z dielectrics and contributing to the production of conduction electrons. High-energy current is a rapid motion of electrons released in the *active* thin layer of the sensor (high-Z cathode), but their transport (motion) occurs mostly in the low-density *passive* dielectric layer without significant loss, as shown in Figures 2B and 3B for the case when the dielectric is air.

75 Thus the roles of “active” and “passive” are reversed compared to their conventional meaning in detector science. For example, in semiconductor detectors the semiconductor is the active medium and electrodes are used to apply an external high voltage and collect charge carriers (electron-hole) generated by radiation interactions. By contrast, in an idealized scenario of vacuum between the high-Z/low-Z conducting layers, the electrodes serve as true emitters and collectors, while for non-vacuum the dielectric becomes a “semiconductor” (or quasi-conductor) not only by the generation of electron hole pairs or other charge carriers but also by virtue of HEC-induced current, which can be likened to an “electric breakdown” current. In the presence of low-Z dielectric, a fraction of the HEC electron energy is always transferred to the dielectric medium creating charge carriers (electrons, positive or negative ions, electron hole pairs), which are self-collected by the electrodes due to the contact potential-induced internal electric field. These latter contributions, but without the presence of the contact potential, are analogous to contributions observed in periodic metal-semiconductor-metal structures¹⁹.

80 Conventional devices interacting with ionizing radiation convert the energy of radiation to operational signal mainly by three methods: (a) by stopping radiation in a scintillating material and measuring the subsequent light emission using optical detectors, e.g., photodiodes (“*indirect conversion*” to light), (b) by stopping radiation in a solid medium (e.g., semiconductor) to generate charge carriers, which are subsequently moved by an electrical field towards the electrodes, forming an electric current in the external circuitry (“*direct conversion*” via conversion to e.g., electron-hole pairs), (c) by stopping radiation in a medium, forming a latent signal (altered physical or chemical state of the medium) to be read by an additional device or mechanism (typically by photostimulation via laser, thermal stimulation, chemical development, or reading of voltage or electrochemical potential). The latter is a very indirect type of conversion, characteristic to passive detectors. Note that the standard use of the term “direct”, as in “*direct conversion*” (case b), is only meant to provide a contrast relative to the “*indirect*” conversion based on scintillators (case a). In that sense, the HEC mechanism via fast electrons introduced in this work is a prompt and truly direct conversion of energy.

85 90 95 100 105 110 115 120 125 130 135 140 145 150 The differences between HEC and standard electric current are several. For example, in a semiconductor detector generating standard current requires a large bias voltage to set the charge carriers in motion towards the electrodes, especially if the active layer thickness is large. There, the semiconductor forms the bulk active volume of the sensor as well as the medium in which the low-energy electric current is generated. In the case of HEC device, the active layer and the transport media are different, and the external electric field is not required, but if applied it could further increase the collection efficiency of the device. Second, the semiconductor detector relies on moving charge carriers (electrons and holes) in a contiguous medium. The higher its density or its atomic number, or the thicker the semiconductor, the greater is the absorption of the radiation, and therefore the efficiency of the sensor. However, the thicker the semiconductor the larger the required bias voltage and the greater the complexity of the device. In detectors used in imaging applications, the increased detector thickness also contributes to the degradation of image quality due to lateral scatter (cross-talk). In the HEC device, the transport medium is a low-density insulator (in extreme case a vacuum cavity or porous material). Unlike in the case of conventional devices, here radiation is mostly stopped not in the medium in which the charge carriers move (which is conventionally the active layer) but in the thin high-Z layer (cathode). The secondary electrons move across the insulating medium towards the low- or medium-Z conducting layer (anode) (Fig 1). Due to the instantaneous induction of the corresponding electric currents in the conducting cathode/anode via basic electromagnetic laws this leads to the signal measured in the external circuit of the sensor. Therefore, decreasing the atomic number, the density, and the thickness of the dielectric (to the limiting condition of vacuum) results in smaller energy dissipation of HEC electrons (Fig 2A versus 2B and Fig 3A versus 3B) and increased efficiency of the HEC detector (Fig 9). This is opposite to the

characteristics of active layers in conventional devices, in which increasing the detection efficiency requires increased size, density and atomic number.

20 Note that HEC can be utilized as the primary means of carrier transport in any low-density solid medium provided that the separation between the cathode and anode is not too large (i.e., the range of HEC electrons in the medium is greater than the separation). Thus, the best efficiency is to be seen in nano- or micro-structures, or in metamaterials having periodic nanostructures with cavities or voids. But increased absolute number of layers or increased thickness of the layers or their Z value results in greater overall absorption of the primary radiation. This
25 also has a degrading effect of self-attenuation impacting low-energy Auger and photoelectrons.

The role of high Z materials in radiation detectors has been investigated so far in the literature from the point of view of the increased energy absorption in the bulk active volume of the detector. For instance, when a scintillator is combined with higher-Z plates this leads to greater energy absorption and higher total scintillation for the same thickness of the scintillator, which in turn leads to smaller scatter of optical photons and better spatial resolution of detector arrays¹³. Similarly, when high-Z scintillators are used, their ability to stop x-rays or gamma photons per unit path is greatly increased. The same holds for semiconductors, because higher effective Z of the semiconductor implies larger absorption per unit path length. On the other hand, the presence of high-Z electrodes in semiconductor detectors can be detrimental because the high density of carriers generated close to the high-Z electrode can lead to the accumulation of space charges and deterioration of electric field, and therefore much lower collection efficiency¹⁴. In the case of low-Z transport media for HEC electrons, accumulation of charges in the dielectric is also possible in principle; however for thin and very low-Z materials (gas or vacuum) it can be minimized.

40 *Comparison to other relevant detection schemes*

There are a few classes of conventional detectors that share some but not all operating principles:

45 (a) *Faraday cup*

The working principle of the HEC device is different from that of the Faraday cup used in beam monitoring¹⁷. The Faraday cup measures an external charged particle beam by placing a conductive beam stopper in its path. The total charge carried by the beam is collected and measured by an ampere meter. Secondary electrons (with respect to primary charged particles) are generated by impact ionization and are collected in the reverse direction only. Further, it is a macroscopic device that has a single conductor cup. By contrast, in the HEC device electrons are 50 internally generated due to interactions with an external photon beam (neutral particles), primarily via photoelectric absorption followed by secondary emissions. Further, in the HEC device there are two or more micro- or nanoscale electrodes of disparate materials separated by a dielectric. Although our proof-of-principle HEC prototype is microscopic², the best device dimension in a multilayer structure is nanoscopic. Detailed nano- and microscale 55 radiation transport simulations presented in this paper show that the most significant contribution to the signal formation is by Auger electrons, while photoelectrons have only a secondary role. In the HEC device, a complex directionally dependent multiple and sequential cascade of Auger emission is generated due to the incident photons and concomitant fluorescent photons. Unlike the Faraday cup in the HEC device the electrode material selection has a nontrivial impact, and can be tuned to the energy of the incident photon beam. The electric current, which is typically measured by the data acquisition system, has very low energy (up to a few eV), whereas the Auger, photo- 60 and gap ionization electrons have much higher energies, in the range of 100 eV to many keV. The low-energy electric current (LEC) is generated in a complex way by the leakage electrons from the electrodes. These phenomena are not utilized in the Faraday cup.

65 (b) *Metal-semiconductor-metal (M-SC-M) periodic structure*

70 The micron-sized periodic structure and the usage of high-Z material is a common feature in HEC detectors and metal-semiconductor-metal (M-SC-M) detectors alike¹⁸⁻²⁰. M-SC-M has been proposed as a multilayer periodic microstructure with the semiconductor operating in the photoconductive or photovoltaic mode¹⁸. However, only the photoconductive mode in Mo-aSi-Ta has been realized experimentally and only with a few layers (0.5µm Mo, 3µm aSi, 0.5µm Ta). In such instruments, small voltage bias resulting in external electric field on the order of 3000 V/cm field was required to gather the charge carriers. Energy deposited in bulk aSi has been computed for varying number of layers using approximate equations. The main effect on which M-SC-M relies is the increased ionization in the bulk aSi active medium.

75 The multilayer HEC structure adds another dimension to the dose enhancement detection approaches employed in M-SC-M. While dose enhancement occurs due to the presence of the high-Z electrodes, an additional high-energy electron current is formed, which is harnessed by the alternating high-Z/low-Z design. Further, and importantly, the HEC design removes the necessity for using external voltage bias and can work with a variety of insulating materials, which are not semiconductors.

80 (c) *Metal microstrip detectors*

Ostensibly similar arrangements to the HEC detector but with very important differences are metal microstrip detectors²¹⁻²². Metal foil detectors made by photo lithography on silicon wafers have been used for high-flux synchrotron beam profile monitoring due to their high radiation tolerance, low bias voltage (~20 V), and relatively high (~5-20 μm) spatial resolution using ~1-2 μm thick strips, making them semi-transparent to the beam. They have been recently proposed for monitoring linac beams²³. However, these detectors do not employ disparate metal layers. Upon irradiation, a positive charge appears at the electrically isolated strip, which is accumulated by a charge Integrator. Because the detector is not self-powered, an external voltage supply is applied to collect charges. When operated in a pixelated arrangement, a low-noise preamplifier mounted on each readout pixel is also required. These detectors have been tested only in very low energy x-rays (18 keV on average) and displayed relatively low sensitivity, as a single secondary electron emission requires 10^4 incident photons.

90 *Simulation results*

95 Simulated currents for various HEC structures (Al-SiO₂-Cu-SiO₂-Al, Al-SiO₂-Au-SiO₂-Al, and periodic Al-air-Au-air-Al-etc) agree with expectations based on general radiation transport theory. Namely, the high Z layers leak electrons on both of their sides (proximal and distal to the incident radiation), and the thinner the high-Z layer the larger the electron escape probability, which results in greater efficiency for the same total thickness of the detector. The optimal layer size depends on the balance of secondary electron production, which is greater in larger thickness, and the leakage of electrons, which is greater in thinner layers. This depends on the incident photon spectrum and on the material selected for the high-Z layer.

100 While in principle x-ray interactions can produce four types of secondary electrons (via photoelectric absorption, Auger emission, Compton scattering, and pair production), the dominant interaction mechanism at kVp energies in high- and medium-Z conductors is the photoelectric effect followed by Auger emission. The relative contribution of photo- and Auger electrons to the HEC signal depends on the incident x-ray energy, the thickness of the high-Z conductors, and that of the dielectric gap. Past Monte Carlo simulations for 100 nanometer layers of gold in water showed that the primary contributions to energy deposition at these scales are from photoelectrons and Auger electrons, with the Auger electron contributions being dominant within about 1 μm from the layers of gold in the water medium¹⁵. Although Auger electrons escaping from nanolayers of gold have ranges in water of up to about 10 μm the most likely ranges are within a few micrometers. In low-Z and low-density media, such as air, this translates to much larger ranges. Therefore, when gas or void are used as low-Z dielectrics in HEC detectors, the contribution of Auger electrons to HEC is expected to be significant.

105 Interestingly, the HEC structure does not have to be as thick as 1300 μm and posses a large number of layers. Based on the simulations (Figure 7), the leakage current is mostly proportional to the incident photon flux at any depth in the detector. Structures with fewer layers stopping very little of the primary radiation (e.g. ~<1%) are conceivable. For these structures the thinner the layers the higher the efficiency as well.

110 *Potential applications*

20 Designing applications for and the utilization of HEC detectors require a non-conventional thought process because many of their characteristics are different, or even opposite, compared to conventional detectors.

25 The material selection and structure of the HEC detector can be adjusted to suit specific needs. For instance, if many micrometer or nanometer-thick layers are used, even though each designed not to result in too much self shielding of the secondary electrons, the total incident beam absorption will be greater than in any individual layer, which will increase the overall efficiency, as shown in Figures 4, 5B and 6B. Depending on the particular application it may or may not be necessary to absorb all or most of the primary radiation. For example, in medical imaging one wishes to detect all x-rays passing through the patient. However, in other medical applications, such as realtime dosimetry during imaging or treatment procedures, it is sufficient or even **desired** to detect only a small amount of

radiation. It remains to be seen if the HEC detection mechanism can be optimized to enable new detectors with greater sensitivity (and contrast) than the presently existing radiation detection devices, or enable miniaturization of detectors, or allow low-power / self-powered devices to operate in conditions otherwise unattainable.

One immediate and natural area of application of HEC detector is in the measurement of dose and dose distribution inside the patient during radiotherapy (e.g., real-time dosimetry) or around personnel during medical procedures. Determination of dose can be realized using external detector arrays or personal sensors or small implantable devices. In all these applications the sensitivity, low- or no power consumption and the compactness permitted by the HEC mechanism are essential. For instance, self-powered sensors are attractive for areas where there is no power: inside patients, or remote locations, or radiation incident areas, to name a few applications.

Ideally, the detector structures should be made of electrode materials with good electro-chemical characteristics such as gold and aluminum. Gold has excellent radiation, mechanical, corrosion, and electrical properties and we envision it as potentially the best material for a manufactured device. However, other materials are also conceivable, such as copper or lead and aluminum. Material selection and pairing may also consider the energies of fluorescent photons with respect to the binding energies of shell electrons to better utilize the resonant cavity-like behavior of disparate structures.

Conclusions

We have computationally shown that secondary high-energy electrons moving through thin high-Z / low-Z multilayer periodic structures can be effectively harnessed for detection of ionizing radiation. The proposed detection mechanism is a direct conversion of energy of the ionizing radiation to usable signal via induction of low energy currents in the conductors that does not require external power supply or amplification. This is a promising mechanism that can become enabling technology for new self-powered or low-power radiation detectors or devices in real-time and *in-vivo*.

Acknowledgement

The authors wish to express their gratitude to Andrew Karella for many useful discussions. This work was supported in part by contract FA8051-15-P-0010 from the Air Force Civil Engineer Center--East, Tyndall AFB, FL.

References

1. Bushberg JT, Seibert JA, Leidholdt Jr EM, Boone JM, *The Essential Physics of Medical Imaging*, Lippincott Williams & Wilkins (2002)
2. Zygmanski P, Shrestha S, Karella A, Sajo E, Prototypes of self-powered radiation detectors employing intrinsic high-energy current (HEC), tentatively accepted *Med Phys* (2015)
3. Leroy C, Rancoita PG, *Principles Of Radiation Interaction In Matter And Detection*, World Scientific (2009)
4. Burke EA, Wall J, Radiation-Induced Low Energy Electron Emission from Metals, *Nuclear Science, IEEE Transactions*, 17, 193-198 (1970)
5. Shields RB, A platinum in-core flux detector, *IEEE Transactions on Nuclear Science*, 20, Atomic Energy Of Canada Ltd., Chalk River (Ontario). Chalk River Nuclear Labs (1970)
6. Goldstein NP, A Comparison Between Calculated and Measured Neutron Sensitivities of a Pt Self-Powered Detector, *IEEE Transactions on Nuclear Science*, 25, 292-295 (1978)
7. Dillin, TA, Huddleston, RE, MacCallum, CJ, Second Generation Analytical Photo-Compton Current Methods, 22, 2549 – 2555 (1975)
8. Lynch GF, Shields RB Coulter PG, Characterization of Platinum Self-Powered Detectors, *IEEE Transactions on Nuclear Science*, 24, 692 – 695, (1977)
9. Goldstein NP, Chen CL, Todt WH, Gamma-Sensitive Self-Powered Detectors and Their Use for in-Core Flux-Mapping, *IEEE Transactions on Nuclear Science* 28, 752-757(1981)
10. Lorence LJJ, Morel JE, CEPXS/ONELD: A one-dimensional coupled electron-photon discrete ordinates code package. Sandia National Laboratories SAND-92-0261C, 1992.
11. Williams ML, Ilas D, Sajo E, Deterministic Photon Transport Calculations in General Geometry for External Beam Radiation Therapy Calculations, *Medical Physics*, 30 (12), pp. 3183-3195 (2003).
12. Halbleib JA, Kensek RP, Mehlhorn TA, Valdez GD, Seltzer SM, Berger MJ, "ITS Version 3.0: The integrated TIGER series of coupled electron/photon Monte Carlo transport codes", pp. 132 (1992)
13. Iniewski K, Semiconductor radiation detection systems, CRC Press (2010)
14. Sellin PJ, Prekas G, Franc J, Grill R, Electric field distributions in CdZnTe due to reduced temperature and x-ray irradiation, *Appl. Phys. Lett.* 96 , 133509 (2010)

15. Zygmanski P, Liu B, Tsiamas P, Cifter F, Petersheim M, Hesser J, Sajo E, Dependence of Monte Carlo microdosimetric computations on the simulation geometry of gold nanoparticles, *Phys Med Biol* 58, 7961-7911 (2013)
 16. Lorence LJ, Morel JE, Valdez GD. Physics guide to CEPXS: A multi-group coupled electron-photon cross-section generating code. Sandia National Laboratory, SAND89-1685, 1989.
 17. Wille K, The Physics of Particle Accelerators, Oxford University Press (2000)
 18. Naruse Y, Hatayama T, Amorphous Silicon Multilayer Radiation Detectors, *IEEE TRANSACTIONS ON NUCLEAR SCIENCE* 36, 1347-1352 (1989)
 19. Zygmanski P, Abkai C, Han H, Shulevich Y, Menichelli D, Hesser H 2014 Towards low-cost, flexible digital detectors for medical dosimetry and radiation safety applications, *JCAMP* 15, 311-326,
 20. Elshahat B, Gil HS, Filip'yev I, Shrestha S, Hesser J, Kumar J, Karellas A, Zygmanski P, Sajo E, Nanometric organic photovoltaic thin film detectors for dose monitoring in diagnostic x-ray imaging, *Med Phys.* 2015 Jul;42(7):4027. doi: 10.1111/1.4922202.
 21. Pugatch V, Ausheva V, Bauer C, Kno KT, Schmelling M, Tkatcha M, Vassilieva Y, Metal foil detectors and their applications, *Nuclear Instruments and Methods in Physics Research A* 535 566–569 (2004)
 22. Pugatch V, Borysova M, Mykhailenko A, Fedorovitch A, Pylypchenko Y, Perevertaylo V, Franz H, Wittenburg K, Schmelling M, Bauer C. Micro-strip metal detector for the beam profile monitoring. *Nuclear Instrum Meth Phys Res A* 581, 531–534 (2007)
 23. Kovalchuk O, Pugatch V, Chaus A, Fedorovich O, Okhrimenko O, Storozhyk D, Campbell M, Tlustos L, Llopard X, Pospisil S, Prezado Y, Renier M. Metal Micro-detectors for Radiation therapy instrumentation. 2011 IEEE Nuclear Science Symposium Conference, 978-1-4673-0120-6 (2011)
 24. Williams ML, Sajo E. Deterministic calculations of photon spectra for clinical accelerator targets, *Med Phys* 291019-28 (2002)

Appendix

CPEXS considers eight aggregate differential cross sections, which appear in the coupled electron-photon Boltzmann transport equation, organized into multi-group Legendre transfer matrices¹⁶. The reactions included in each of these transfer matrices are summarized in Table 1.

Table 1. Reactions in eight aggregate differential cross-sections, considered by CEPXS. Arrows indicate transfer matrices. e^- = electron, e^+ = positron, p = photon. Adapted from reference 16.